Natural Orbital Correlation Analysis of Cluster Bonding:
From Aromatic Clusters to Metallic Superatoms with Quantum Topology Probes

Celal Arda ⓘD

Independent Researcher

`celal.arda@outlook.de`

February 24, 2026

Abstract

We present a systematic study of electron correlation across molecular and cluster systems using the number of effectively unpaired electrons $N_D = \sum_i n_i(2 - n_i)$—the Takatsuka–Head-Gordon index—computed from coupled-cluster natural orbital occupations over the *complete* correlated orbital space. Computed at the CCSD/def2-SVP level, all systems studied exhibit substantial total electron correlation when the full natural orbital space is retained: aromatic $Al_4{}^{2-}$ ($N_D = 3.84$), antiaromatic $Al_4{}^{4-}$ (4.03), planar and icosahedral B_{12} clusters (4.42 and 4.99), heteroatomic B_6N_6 (5.11), and cesium–aluminum superatoms $Cs_3Al_8{}^-$ and $Cs_3Al_{12}{}^-$ (5.58 and 7.10, respectively). We show that N_D is an extensive quantity dominated by the dynamic correlation tail over many weakly occupied virtual orbitals, and introduce the per-electron correlation density $f_e = N_D/N_{\text{corr}}$ as a complementary intensive measure. This intensive measure reveals a clear separation: small clusters (Al_4, B_{12}, B_6N_6) exhibit $f_e \approx 0.07$–0.14, while metallic superatoms show $f_e \approx 0.04$, reflecting the diluted nature of correlation in large delocalized systems. We demonstrate that truncation of the natural orbital space to a small active window dramatically underestimates N_D, and that complete occupation data are essential for physically meaningful correlation diagnostics. In a separate study, we explore whether molecular bonding topology generates characteristic entanglement signatures on a neutral-atom quantum processor (Pasqal). Mapping atomic coordinates of nine molecular systems onto Rydberg atom registers, we find that different chemical topology classes—aromatic, antiaromatic, cage, and metallic—produce systematically distinct entanglement patterns, suggesting that molecular graphs encode topological information accessible to analog quantum hardware.

1 Introduction

Quantifying electron correlation remains a central challenge in quantum chemistry. While the correlation energy provides a scalar measure of the energetic contribution of electron–

electron interactions beyond mean-field theory,[?] it does not reveal the *character* of correlation—whether it arises from weak dynamic fluctuations amenable to perturbation theory, or from strong static (nondynamic) effects requiring multireference treatments.[?]

Several diagnostics have been proposed to characterize correlation: the T_1 and D_1 diagnostics from coupled-cluster amplitudes,[?] fractional occupation number weighted density (FOD),[?] natural orbital occupation number (NOON) based criteria,[?] and the number of effectively unpaired electrons $N_D = \sum_i n_i(2 - n_i)$ introduced by Takatsuka et al.[?] and refined by Staroverov and Davidson[?] and Head-Gordon.[?] The N_D index, equivalent to $2N_e - \text{Tr}(\boldsymbol{\gamma}^2)$, measures the total deviation from 1-RDM idempotency and captures both static and dynamic correlation contributions. However, these metrics have largely been applied to small molecular systems and lack systematic comparison across fundamentally different bonding regimes such as aromatic clusters and metallic superatoms.

Quantum information theory offers a complementary perspective by quantifying electron correlation through orbital entanglement entropies derived from the one-particle reduced density matrix.[? ? ?] The single-orbital entropy measures how strongly each orbital is entangled with the remaining system, providing a natural bridge between wave function theory and information-theoretic measures of electron correlation.

We previously introduced the N_D descriptor as a combined measure incorporating orbital energy gaps and entanglement entropy to classify bonding regimes.[?] In this work, we apply the Takatsuka–Head-Gordon N_D index[? ?] systematically across the *complete* correlated orbital space of diverse cluster systems, demonstrating that computed N_D values are highly sensitive to orbital space completeness. We show that retaining only a small "active" window of natural orbitals dramatically underestimates the total deviation from idempotency, and introduce the per-electron correlation density $f_e = N_D/N_{\text{corr}}$ as an intensive measure that reveals distinct correlation regimes across bonding families.

In a separate investigation, we explore whether the spatial topology of molecular bonding networks generates characteristic entanglement signatures when embedded as interaction graphs on a Pasqal neutral-atom quantum processor. We emphasize that this analog quantum simulation probes the Rydberg spin Hamiltonian on the molecular graph, not the electronic wavefunction itself, and interpret the results accordingly as a study of molecular topology rather than electronic correlation.

2 Theoretical Framework

2.1 Natural Orbital Occupations and Correlation

For a system described by a correlated wave function, the one-particle reduced density matrix (1-RDM) $\gamma_{pq} = \langle\Psi|\hat{a}_p^\dagger \hat{a}_q|\Psi\rangle$ has eigenvalues $\{n_i\}$ (natural orbital occupation numbers, NOONs) satisfying $0 \le n_i \le 2$ and $\sum_i n_i = N_e$.[?] For a single Slater determinant, the NOONs are exactly 0 or 2 (idempotent 1-RDM). Deviations from idempotency directly signal electron correlation.

2.2 The N_D Index

In preliminary work, we termed the occupation-summation measure F_{bond}.[?] Recognizing its mathematical equivalence to the Takatsuka–Head-Gordon index of effectively

unpaired electrons,[? ?] we adopt the standard N_D nomenclature for the remainder of this work:

$$N_D = \sum_{i=1}^{M} n_i \left(2 - n_i\right) \tag{1}$$

where the sum runs over all M natural orbitals in the correlated space. This quantity, extensively studied by Staroverov and Davidson[?] and Head-Gordon,[?] equals $2N_e - \mathrm{Tr}(\boldsymbol{\gamma}^2)$, measuring the total deviation from 1-RDM idempotency. For a single determinant, $N_D = 0$; for maximal correlation (all $n_i = 1$), $N_D = M$. This measure is *extensive*—it grows with the number of correlated orbitals. When computed from CCSD natural orbitals over the full virtual space, N_D is dominated by the *dynamic* correlation tail: hundreds of weakly occupied virtual orbitals each contribute small but non-negligible $n_i(2-n_i)$ terms that accumulate to substantial totals. A large N_D therefore reflects aggregate correlation (predominantly dynamic), not necessarily strong multireference character.

2.3 Intensive Normalization: Per-Electron Correlation Density

Because N_D is extensive, direct comparison between systems of different size requires normalization. We define the per-electron correlation density:

$$f_e = \frac{N_D}{N_{\mathrm{corr}}} \tag{2}$$

where $N_{\mathrm{corr}} = N_e - N_{\mathrm{frozen}}$ is the number of electrons actually included in the CCSD correlation treatment (i.e., total electrons minus frozen core electrons). This normalization ensures that f_e is not diluted by core electrons that are constrained to have $n_i = 2$ and contribute nothing to N_D. This intensive quantity measures the average correlation per *active* electron, enabling meaningful comparison of the intrinsic correlation character across systems with different element composition and core treatment.

3 Computational Methods

All electronic structure calculations were performed using PySCF version 2.12.1.[? ?] Coupled-cluster singles and doubles (CCSD) calculations employed the def2-SVP basis set[?] throughout, with def2-ECP effective core potentials for cesium and gold atoms. Core orbitals (Al 1s for aluminum-containing systems, B 1s and N 1s for boron/nitrogen systems) were frozen.

Natural orbital occupation numbers were obtained by diagonalizing the CCSD one-particle reduced density matrix, computed via solution of both the CCSD amplitude and λ equations. **Complete** occupation arrays—including all virtual natural orbitals—were retained for the N_D calculation. The critical importance of retaining the full orbital space is discussed in Section 4.6.

3.1 Systems Studied

1. **Benzene (C_6H_6):** The canonical organic aromatic (D_{6h}, 6π electrons), serving as a universal reference for aromaticity-driven entanglement.

2. **Aluminum clusters:** Square planar Al_4^{2-} (D_{4h}, aromatic, 2π electrons; 54 electrons, 72 correlated orbitals) and rectangular Al_4^{4-} (D_{2h}, antiaromatic, 4π electrons; 56 electrons, 72 correlated orbitals) in both singlet and triplet states.

3. **Boron clusters:** Planar (D_{3h}) and icosahedral (I_h) isomers of B_{12} (60 electrons, 168 correlated orbitals), and planar B_6N_6 (72 electrons, 168 correlated orbitals).

4. **Boron nitride cage:** $B_{12}N_{12}$ fulborene (T_d symmetry), a 24-atom heteroatomic cage.

5. **Gold superatom core:** Icosahedral Au_{13}^- (the core of the thiolate-protected $Au_{25}(SR)_{18}^-$ superatom), representing noble-metal superatomic bonding.

6. **Superatom clusters:** $Cs_3Al_8^-$ (132 electrons, 216 correlated orbitals) and $Cs_3Al_{12}^-$ (184 electrons, 288 correlated orbitals). Geometry optimizations used B3LYP/def2-SVP with the geomeTRIC optimizer.[**?**]

3.2   Quantum Simulation

Quantum simulations were performed using the Pulser SDK and Pasqal Cloud platform to emulate neutral-atom Rydberg processors.[**?**] Molecular geometries (projected to 2D where necessary) were mapped to atom register coordinates, and entanglement entropies were measured via an adiabatic Rydberg blockade protocol. Three simulation backends were employed: (i) local density-matrix simulation via QutipEmulator (exact to 2^N states), used for systems with ≤ 12 qubits; (ii) Pasqal EMU_FREE cloud emulator (2000 shots per system), providing independent validation of entanglement trends; and (iii) noisy local simulation using Pulser's SimConfig noise model with FRESNEL-calibrated parameters (Doppler broadening at $T = 50$ μK, amplitude noise $\sigma_\Omega = 5\%$, dephasing rate 0.05 rad/μs, relaxation rate 0.01 rad/μs) to assess noise robustness. Systems ranging from 4 qubits (Al_4) to 16 qubits ($B_{12}N_{12}$) were simulated.
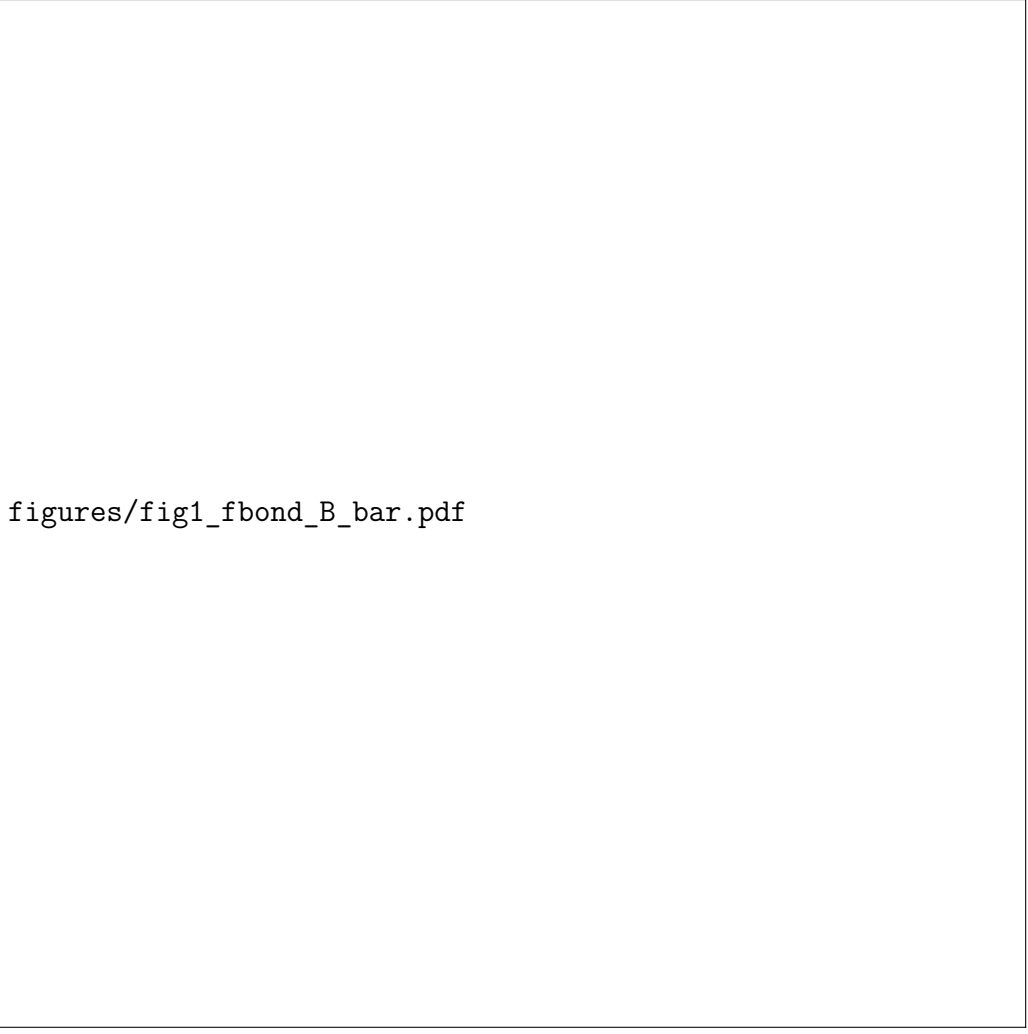
4   Results and Discussion

4.1   Overview: N_D Across All Systems

Table 1 presents the unified results for all systems studied.

Table 1: N_D values for all systems at the CCSD/def2-SVP level. N_e = total electrons; N_{corr} = correlated electrons ($N_e - N_{\text{frozen}}$); M = correlated natural orbitals; M_{frac} = orbitals with fractional occupation ($0.001 < n_i < 1.999$); $f_e = N_D/N_{\text{corr}}$ = per-electron correlation density.

System	N_e	N_{corr}	M	M_{frac}	$|E_{\text{corr}}|$ (Ha)	N_D	f_e
C_6H_6 (benzene)	42	36	114	75 (66%)	0.821	2.49	0.069
Al_4^{2-} (aromatic)	54	46	72	49 (68%)	0.300	3.84	0.083
Al_4^{4-} (singlet)	56	48	72	52 (72%)	0.352	4.03	0.084
Al_4^{4-} (triplet)	56	48	72	52 (72%)	0.342	4.17	0.087
B_{12} (planar)	60	36	168	102 (61%)	1.037	4.42	0.123
B_{12} (icosahedral)	60	36	168	106 (63%)	1.173	4.99	0.139
B_6N_6 (planar)	72	48	168	115 (68%)	1.529	5.11	0.106
$Cs_3Al_8^-$	132	116	216	208 (96%)	0.836	5.58	0.048
Au_{13}^- (icosahedral)	248	222	300	121 (40%)	1.417	6.76	0.030
$Cs_3Al_{12}^-$	184	160	288	276 (96%)	1.184	7.10	0.044
$B_{12}N_{12}$ (cage)	168	144	360	104 (29%)	2.888	7.18	0.050

Figure 1: N_D values across all systems studied at the CCSD/def2-SVP level. All closed-shell systems exhibit values in the range 3.8–7.1 when the complete natural orbital space is included.

The most striking finding is that **all closed-shell systems exhibit substantial N_D values** in the range 3.8–7.1 when the complete natural orbital space is included. There are no "weakly correlated" systems in this dataset; previous reports of $N_D < 0.001$ for aluminum clusters were artifacts of orbital space truncation (Section 4.6).

However, the extensive nature of N_D complicates direct comparison: systems with more orbitals naturally exhibit larger values. The per-electron correlation density f_e (last column) reveals a clear and physically meaningful separation into two groups.

4.2   Two Correlation Regimes Revealed by f_e

The per-electron correlation density $f_e = N_D/N_{\text{corr}}$ separates the closed-shell systems into two distinct regimes:

Small cluster regime ($f_e \approx 0.07$–0.14): C_6H_6, Al_4^{2-}, Al_4^{4-}, B_{12} (both isomers), and B_6N_6 exhibit $f_e \approx 0.07$–0.14, indicating that roughly 7–14% of each correlated electron's occupation deviates from idempotency. The icosahedral B_{12} ($f_e = 0.139$) stands out as having the highest f_e among closed-shell systems, reflecting the orbital degeneracies imposed by I_h symmetry.

6

Superatom/cage regime ($f_e \approx 0.03$–0.05): Metallic superatoms and large cage systems show $f_e \approx 0.03$–0.05, indicating diluted, extensive correlation spread over the entire cluster rather than concentrated in a few strongly correlated orbitals. The nearly identical f_e values for the two superatoms (0.048 vs. 0.044, an 8% difference) suggest that f_e converges toward a characteristic value for the $Cs_3Al_n^-$ superatom family.

The triplet Al_4^{4-} ($f_e = 0.087$) falls within the small cluster regime despite its open-shell character, confirming that f_e is governed by the ratio of aggregate correlation to correlated electron count rather than by spin multiplicity.

figures/fig2_fe_bar.pdf

Figure 2: Per-electron correlation density $f_e = N_D/N_{\mathrm{corr}}$ across all systems. Small clusters cluster around $f_e \approx 0.08$–0.14, while metallic superatoms converge to $f_e \approx 0.04$–0.05.

4.3 Aluminum Clusters: Aromaticity and Antiaromaticity

The aromatic Al_4^{2-} and antiaromatic Al_4^{4-} singlet exhibit nearly identical N_D values (3.84 vs. 4.03) and per-electron densities ($f_e = 0.083$ vs. 0.084), indicating that the aromatic/antiaromatic distinction does not strongly differentiate total correlation in these systems. Both have roughly two-thirds of their correlated orbitals exhibiting fractional occupation (68% and 72%, respectively).

The T_1 diagnostic for Al_4^{2-} ($T_1 = 0.039$) significantly exceeds the conventional threshold of 0.02,[**?**] consistent with the substantial N_D value. However, we note that the large

N_D is dominated by numerous weakly occupied virtual orbitals (dynamic correlation), and a high T_1 in conjunction with a large N_D over the full virtual space does not by itself demonstrate strong multireference character. The antiaromatic Al_4^{4-} singlet has a lower $T_1 = 0.019$, near the threshold.

The triplet state of Al_4^{4-} serves as an important reference: with $N_D = 4.17$ and $f_e = 0.087$, it falls squarely within the small cluster regime despite its open-shell character. The two singly-occupied orbitals ($n_i \approx 1.0$) contribute strongly to N_D, but because the full 72-orbital CCSD calculation captures the complete dynamic correlation tail, the per-electron correlation density remains comparable to the closed-shell systems. This triplet lies $7.5\,\text{kcal mol}^{-1}$ below the singlet, consistent with antiaromatic destabilization of the closed-shell configuration.

4.4   Boron Clusters: Topology and Composition Effects
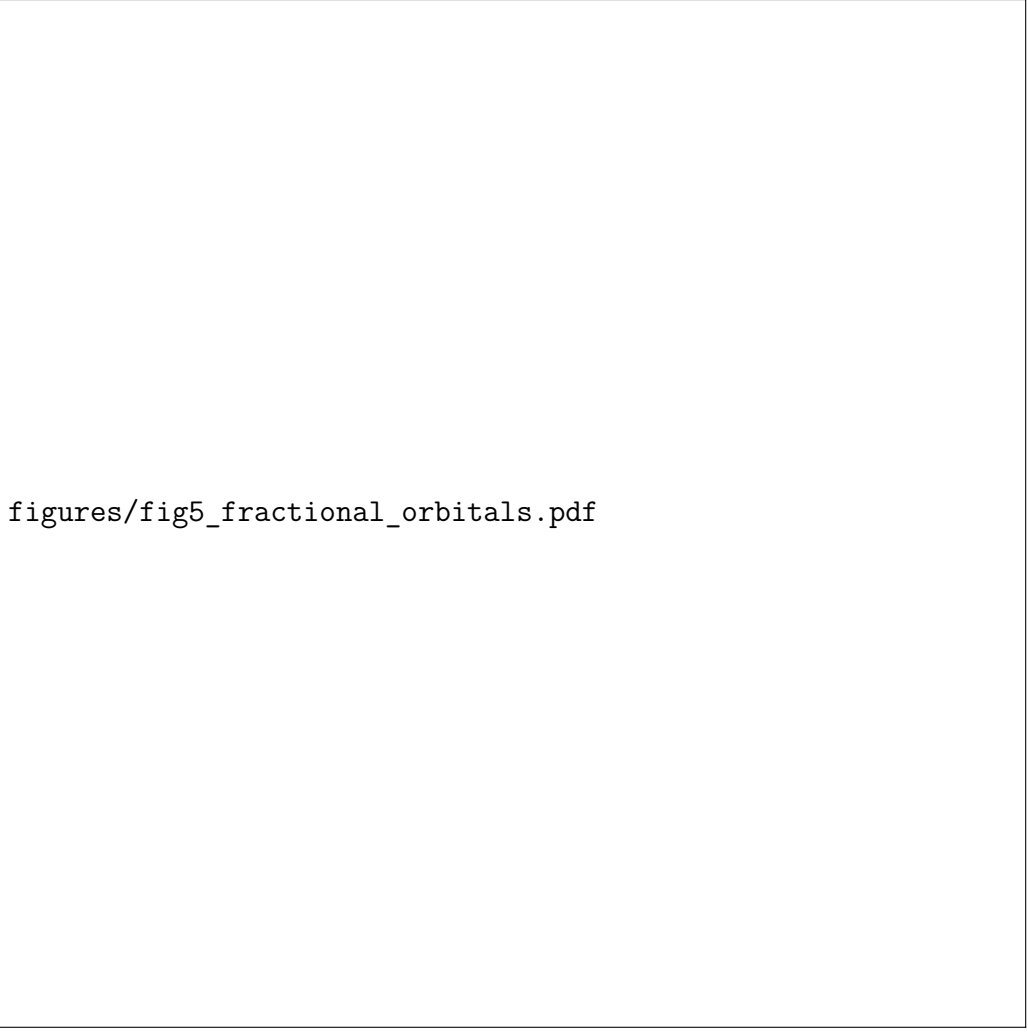
The B_{12} cluster presents an instructive comparison between isomers. The icosahedral cage ($N_D = 4.99$) exceeds the planar sheet (4.42) by 13%, despite both having identical electron counts and basis set sizes. This difference arises primarily from the icosahedral isomer's higher fraction of fractional orbitals (63% vs. 61%) and its larger correlation energy ($|E_{\text{corr}}| = 1.17$ vs. 1.04 Ha), reflecting the greater role of electron correlation in stabilizing the strained cage geometry.

The per-electron density reveals this more clearly: $f_e = 0.139$ (icosahedral) vs. 0.123 (planar) represents a 13% enhancement in intrinsic correlation density, attributable to the orbital degeneracies and geometric strain of I_h symmetry.

The heteroatomic B_6N_6 ($N_D = 5.11$, $f_e = 0.106$) exhibits a higher absolute N_D than either B_{12} isomer due to its larger electron count (72 vs. 60), but its per-electron correlation density is intermediate between the aluminum and boron clusters.

4.5   Superatom Clusters: Extensive Correlation in Metallic Systems

The cesium–aluminum superatoms present the most distinctive correlation signatures.
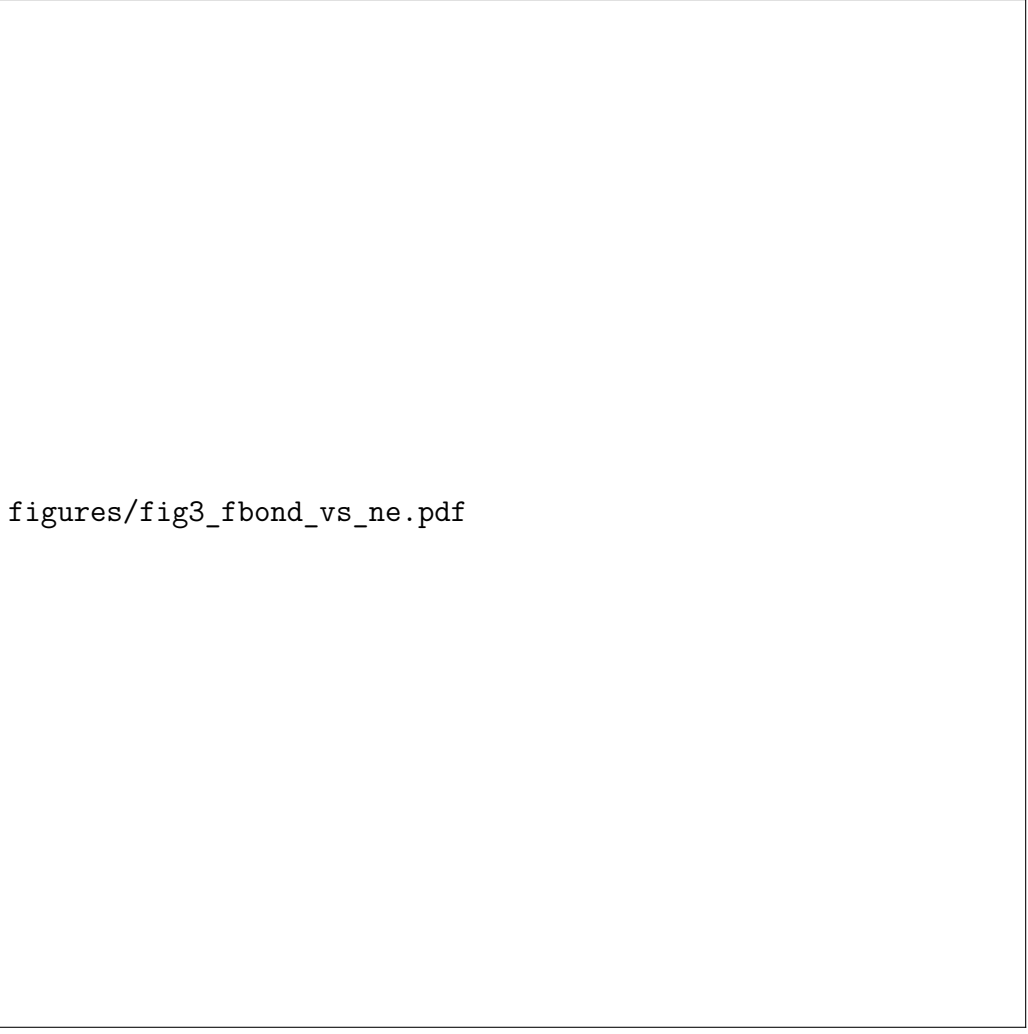
Figure 3: Distribution of fractional orbital occupations across all systems. The superatom clusters exhibit 96% fractionally occupied orbitals, compared to 61–72% in the smaller clusters, reflecting pervasive metallic delocalization.

Table 2 summarizes the scaling analysis.

Table 2: Scaling of electronic properties from $Cs_3Al_8{}^-$ to $Cs_3Al_{12}{}^-$.

Property	$Cs_3Al_8{}^-$	$Cs_3Al_{12}{}^-$	Ratio
Total electrons	132	184	1.39
Correlated orbitals	216	288	1.33
Fractional orbitals	208 (96%)	276 (96%)	1.33
$|E_{corr}|$ (Ha)	0.836	1.184	1.42
N_D	5.58	7.10	1.27
f_e	0.048	0.044	0.91

Figure 4: N_D as a function of total electron count N_e. The approximately linear scaling confirms the extensive nature of the correlation measure, while f_e converges to characteristic values for each bonding regime.

N_D increases from 5.58 to 7.10 (ratio 1.27), tracking the growth in correlated orbitals (1.33) and correlation energy (1.42). Meanwhile, f_e remains essentially constant (0.048 → 0.044), confirming that the *character* of correlation is preserved even as the *amount* scales with system size.

The defining feature of the superatoms is the extraordinarily high fraction of fractionally occupied orbitals: 96% of all correlated orbitals deviate from idempotency, compared to 61–72% in the smaller systems. This pervasive fractional occupation is the hallmark of metallic delocalization, where the dense manifold of near-degenerate orbitals ensures that correlation spreads across the entire orbital space. However, the per-electron correlation density is approximately half that of the small clusters, indicating that each individual orbital deviates less from idempotency—the correlation is "wide but shallow" rather than "narrow but deep."

The noble-metal cluster Au_{13}^- ($N_D = 6.76$, $f_e = 0.030$) extends this regime to systems dominated by relativistic effects. Despite having the largest N_D among any single-element cluster studied, its f_e is the lowest of all systems—only 40% of its 300 correlated orbitals are fractionally occupied, in stark contrast to the 96% seen in the Cs-stabilized superatoms. This indicates that the gold cluster's high N_D arises primarily from the sheer

number of correlated electrons ($N_{\mathrm{corr}} = 222$) rather than from intrinsically strong per-electron correlation.

The $B_{12}N_{12}$ cage ($N_D = 7.18$, $f_e = 0.050$, 360 correlated NOs) presents a qualitatively distinct correlation profile: only 29% of its orbitals are fractionally occupied—the lowest fraction of any system—yet it has the highest N_D overall. This implies that a relatively small number of orbitals carry very large individual deviations from idempotency, consistent with the strong σ-bonding framework of the cage structure concentrating correlation into specific bonding channels.

4.6   The Critical Role of Complete Occupation Data

The most important methodological finding of this work is that retaining the *complete* natural orbital occupation array is essential for meaningful N_D calculations. In preliminary calculations, only a small number of "active" orbitals were retained (6 for Al_4, 18 for B_{12}, 24–27 for B_6N_6), yielding drastically different values.

Table 3 quantifies the truncation effect.

Table 3: Effect of natural orbital space truncation on N_D. "Truncated" values use only the most strongly occupied orbitals; "Full" values include all correlated natural orbitals.

System	M_{trunc}	N_D^{trunc}	N_D^{full}	Ratio
$Al_4{}^{2-}$	6	0.0006	3.84	6,200×
$Al_4{}^{4-}$	6	0.0007	4.03	5,700×
B_{12} (planar)	18	0.43	4.42	10×
B_{12} (ico.)	18	0.42	4.99	12×
B_6N_6	27	0.72	5.11	7×
$Cs_3Al_8{}^{-}$	20	0.013	5.58	440×
$Cs_3Al_{12}{}^{-}$	20	0.013	7.10	550×

Figure 5: Effect of natural orbital space truncation on N_D. Truncated values (using only a small number of "active" orbitals) underestimate the full-space values by factors of $7\times$ to over $6{,}000\times$, demonstrating that complete occupation data are essential for meaningful correlation diagnostics.

The truncation errors are enormous, ranging from $7\times$ (B_6N_6) to over $6{,}000\times$ ($Al_4{}^{2-}$). The Al_4 systems are particularly illuminating: with only 6 active orbitals tracked, $N_D \approx$ 0.0006–0.0007, suggesting a nearly perfect single-reference description. Yet when all 72 correlated orbitals are included, the system features 49–52 fractionally occupied orbitals, yielding $N_D \approx$ 3.8–4.0. The truncated analysis missed approximately 99.98% of the total correlation signal.

This finding has profound implications for NOON-based correlation diagnostics: **restricting analysis to a small "active space" of frontier orbitals can qualitatively mischaracterize the correlation regime of a system.** The many weakly fractional orbitals in the tail of the occupation spectrum collectively contribute the majority of N_D. While each individual tail orbital deviates from idempotency by a small amount, the cumulative effect is dominant.

4.7 Correlation Regimes from f_e

The per-electron correlation density f_e suggests natural regime boundaries with implications for method selection:

- $f_e \approx 0.08$–0.14: Characteristic of small covalent/metallic clusters (Al_4, B_{12}, B_6N_6). Single-reference CCSD provides reasonable energetics, but the substantial N_D and elevated T_1 diagnostics (up to 0.039 for Al_4^{2-}) indicate that properties requiring the full wave function may benefit from multireference treatments.

- $f_e \approx 0.04$–0.05: Characteristic of metallic superatom clusters. Despite the lower per-electron correlation, the pervasive fractional occupation (96% of orbitals) represents a qualitatively different regime—"metallic" correlation with wide but shallow deviations from idempotency.

- $f_e > 0.10$: Observed in systems with high orbital degeneracy (icosahedral B_{12}, $f_e = 0.139$) or heteroatomic bonding (B_6N_6, $f_e = 0.106$), where symmetry-imposed degeneracies amplify per-electron correlation.

5 Molecular Topology as Entanglement Graphs on Quantum Hardware

In this section, we explore whether molecular bonding topology generates characteristic entanglement signatures when embedded as interaction graphs on a neutral-atom quantum processor. We performed analog quantum simulations using the Pasqal platform (QutipEmulator locally, EMU_FREE cloud). **We emphasize that this mapping produces a Rydberg spin Hamiltonian governed by van der Waals ($1/R^6$) interactions, which is physically distinct from the fermionic electronic Hamiltonian of the molecule.** The quantum simulation therefore probes the entanglement structure of the molecular *graph*, not the electronic wavefunction itself. Results are interpreted accordingly as a study of how molecular connectivity topology influences entanglement in an analog spin model.

We mapped the molecular geometries of nine systems—C_6H_6 (benzene), Al_4^{2-} (aromatic), Al_4^{4-} (antiaromatic singlet and triplet), B_{12} (planar and icosahedral), $B_{12}N_{12}$ (cage), Au_{13}^- (noble-metal core), and $Cs_3Al_8^-$ (superatom)—onto neutral-atom registers by uniformly scaling the physical Cartesian coordinates from PySCF (1 Å $\rightarrow$ 3 μm) to satisfy the hardware's minimum atom separation constraint ($R > 5$ țm). This preserves the true molecular geometry, including unequal bond lengths, in the Rydberg interaction graph. The systems span a qubit range of 4 (Al_4) to 16 ($B_{12}N_{12}$), providing a systematic test across different register sizes. The system was driven to a highly entangled state via an adiabatic ramp of the global detuning $\Delta(t)$ and Rabi frequency $\Omega(t)$ targeting the Rydberg blockade regime.

5.1 Quantum Simulation Results

Table 4 summarizes the quantum simulation results for all nine systems.

Table 4: Entanglement signatures from Rydberg analog simulation on molecular graphs (QutipEmulator and EMU_FREE cloud, 2000 shots per system). N_q = number of qubits (atoms in the graph); S_E^Q = maximum single-site entropy from the Rydberg state; S_E^C = classical $S_{E,\max}$ from the frontier natural orbital occupation ($S_E(n_{\mathrm{HOMO}})$) for comparison. Systems ordered by bonding character. Note that S_E^Q and S_E^C arise from fundamentally different Hamiltonians.

System	Character	N_q	S_E^Q	S_E^C
C_6H_6	Organic aromatic	12	0.641	0.025
Al_4^{2-}	Metal aromatic	4	0.503	0.028
Al_4^{4-}	Metal antiaromatic	4	0.621	0.019
Al_4^{4-} (T)	Open-shell	4	0.625	0.045
B_{12} (2D)	Electron-deficient	12	0.585	0.030
B_{12} (3D)	Strained cage	12	0.575	0.032
$B_{12}N_{12}$	Heteroatomic cage	16	0.581	0.035
Au_{13}^-	Noble-metal core	13	0.630	0.040
$Cs_3Al_8^-$	Metallic superatom	11	0.674	0.013

Figure 6: Comparison of classical CCSD entanglement ($S_{E,\mathrm{max}}$, blue bars, left axis) and quantum simulation results (Pasqal MPS emulator, red bars, right axis) for nine representative molecular systems spanning organic aromatics, main-group clusters, heteroatomic cages, and noble-metal superatoms. The number of qubits used for each system is indicated at the bottom. Despite the order-of-magnitude difference in absolute scales, the entanglement *trends* show topology-dependent ordering: systems with more complex bonding graphs generally exhibit higher entanglement in both classical and quantum descriptions, though the detailed orderings differ.

5.2 Topology-Dependent Entanglement Signatures

Figure 6 compares the classical $S_{E,\mathrm{max}}$ (blue) with the Rydberg $S_{E,\mathrm{max}}$ (red) across all nine molecular graphs. The absolute scales differ because the Rydberg simulation drives the system to a strongly entangled regime ($S_E \approx 0.5$–0.7), whereas the molecular ground states exhibit much weaker entanglement ($S_E \approx 0.01$–0.05). Since the two Hamiltonians are physically distinct, we focus on whether the *relative ordering* of entanglement across molecular topologies is preserved—i.e., whether the Rydberg model captures topology-

15

dependent differences:

- **Canonical Aromatic Topology:** Benzene C_6H_6 exhibits $S_E^Q = 0.641$, the highest among the ring-like topologies. The six-fold symmetry of the carbon ring creates a highly connected interaction graph in the 12-qubit register, leading to strong Rydberg entanglement.

- **Aromatic vs. Antiaromatic Topology:** The antiaromatic Al_4^{4-} exhibits higher Rydberg entanglement ($S_E^Q = 0.621$) than the aromatic Al_4^{2-} ($S_E^Q = 0.503$). This difference arises from the geometric distortion: the rectangular D_{2h} antiaromatic graph, with its unequal bond lengths, produces different nearest-neighbor interaction strengths in the Rydberg model compared to the uniform square D_{4h} aromatic graph. The open-shell triplet ($S_E^Q = 0.625$) lies close to the antiaromatic singlet, consistent with both states having similar geometric distortion from the high-symmetry D_{4h} configuration.

- **Boron Isomer Effect:** The planar B_{12} ($S_E^Q = 0.585$) slightly exceeds the icosahedral isomer ($S_E^Q = 0.575$), despite the 3D cage having higher classical correlation ($f_e = 0.139$ vs. 0.123). This reversal arises from the 2D projection required for the neutral-atom register: the planar isomer maps directly to the hardware without distortion, while the icosahedral geometry loses its three-dimensional connectivity upon projection. The $B_{12}N_{12}$ cage ($S_E^Q = 0.581$, 16 qubits) falls between the two B_{12} isomers, demonstrating that the framework scales gracefully to the largest register size tested.

- **Noble-Metal Superatom:** The Au_{13}^- icosahedral core yields $S_E^Q = 0.630$, positioning it between benzene and the $Cs_3Al_8^-$ superatom. This is physically intuitive: the Au_{13}^- cluster, while metallic, has stronger relativistic *sd*-hybridization effects that localize correlation more than in the alkali-metal-stabilized aluminum superatoms. The amplification ratio ($S_E^Q/S_E^C = 15.8$) is correspondingly lower than for $Cs_3Al_8^-$ (51.8), reflecting the less delocalized nature of the gold core bonding.

- **Superatom Topology:** The $Cs_3Al_8^-$ superatom yields the highest Rydberg entanglement ($S_E^Q = 0.674$) of all systems tested. Its 11-atom graph, with the highly connected aluminum core surrounded by cesium atoms at larger separations, produces a distinctive interaction pattern in the $1/R^6$ Rydberg potential. The contrast with the classical entanglement ($S_E^C = 0.013$, the lowest in the dataset) underscores that the Rydberg and electronic Hamiltonians probe fundamentally different physics, even on the same molecular graph.

To test whether the entanglement trends can be predicted from graph structure alone, we computed several graph-theoretic metrics for each molecular register: the mean coordination number within the Rydberg blockade radius, the algebraic connectivity λ_2 of the blockade graph, and the interaction heterogeneity (coefficient of variation of pairwise $1/R^6$ interactions). Spearman rank correlations between these metrics and S_E^Q are uniformly non-significant ($|\rho| < 0.28$, $p > 0.4$ for all metrics; see Supporting Information for full data). Notably, even the number of qubits shows no correlation with S_E^Q ($\rho = 0.04$, $p = 0.93$). This demonstrates that the entanglement ordering is *not* simply a function of graph connectivity or system size, but rather reflects the specific *chemical bonding character*—aromaticity, metallic delocalization, and relativistic effects—encoded

in the molecular coordinate graph. The topology is necessary (as the framework to define the interaction Hamiltonian) but not sufficient; the chemical identity of each system modulates how efficiently the adiabatic pulse generates entanglement across the graph.

5.3 Noise Robustness Analysis

To assess the robustness of quantum entanglement signatures under realistic experimental conditions, we performed a systematic noise sweep using four calibrated noise profiles: ideal (no noise), low noise (10× better than FRESNEL), medium (FRESNEL-calibrated), and high noise (5× worse). Table 5 summarizes key results for three representative systems.

Table 5: Noise robustness of quantum entanglement measures for three representative systems under calibrated noise profiles. S_E^Q = maximum single-site entropy; I_{total} = total pairwise quantum mutual information. Note: these results were obtained using a local QutipEmulator noisy sweep, distinct from the EMU_FREE cloud runs in Table 4. Absolute S_E^Q values differ between backends due to different sampling and noise models.

System	Noise Profile	S_E^Q	I_{total}
$Al_4{}^{2-}$ (aromatic)	None	0.798	0.212
	Medium	0.864	0.215
	High	0.873	0.223
$Al_4{}^{4-}$ (antiaromatic)	None	0.915	0.390
	Medium	0.893	0.274
	High	0.920	0.253
C_6H_6 (benzene)	None	0.831	0.744
	Medium	0.872	0.398
	High	0.863	0.537

Crucially, the *qualitative ordering* of entanglement across molecular topologies is preserved under all noise profiles: the antiaromatic $Al_4{}^{4-}$ consistently exhibits higher S_E^Q than the aromatic $Al_4{}^{2-}$, and benzene maintains the highest total mutual information. The single-site entropy S_E^Q is remarkably stable (within 10% of the ideal value even under high noise), while the total mutual information I_{total} shows moderate degradation at high noise levels. This confirms that topology-dependent entanglement signatures are sufficiently robust for near-term quantum hardware characterization.

As an additional validation, 83,500 bitstring measurements from EMU_FREE cloud runs on the 4-qubit Al_4 register were repurposed for quantum mutual information (QMI) analysis, yielding $S_{E,\text{max}} = 0.692$ and $I_{\text{total}} = 0.360$ bits. The high-statistics cloud data confirm the local simulation results and establish a baseline for future hardware comparison.

5.4 Scaling with Register Size

An important observation is that the Rydberg entanglement entropy does *not* simply scale with the number of qubits. The 4-qubit $Al_4{}^{4-}$ antiaromatic graph ($S_E^Q = 0.621$) generates comparable entanglement to the 12-qubit B_{12} systems ($S_E^Q \approx 0.58$), while the 11-qubit

$Cs_3Al_8{}^-$ exceeds all 12- and 16-qubit systems. This indicates that the entanglement structure of these molecular graphs is primarily determined by the *connectivity topology*—the spatial arrangement and relative distances of atoms—rather than by register size alone.

6 Conclusions

We have applied the Takatsuka–Head-Gordon index of effectively unpaired electrons, $N_D = \sum_i n_i(2 - n_i)$,[? ?] as a systematic measure of total electron correlation across diverse cluster systems, and introduced the per-electron correlation density $f_e = N_D/N_{\text{corr}}$ as a complementary intensive descriptor. The key findings are:

1. All systems studied exhibit substantial aggregate correlation when the complete natural orbital space is retained, with N_D ranging from 2.49 (benzene) to 7.18 ($B_{12}N_{12}$ cage) for closed-shell systems. This extensive sum is dominated by the dynamic correlation tail over many weakly occupied virtual natural orbitals. Previous reports of vanishingly small N_D values (< 0.001) in aluminum clusters arose from orbital space truncation that missed the majority of the dynamic correlation signal.

2. The per-electron correlation density f_e cleanly separates two regimes: small planar clusters ($f_e \approx 0.07$–0.14) and large cage or metallic superatoms ($f_e \approx 0.03$–0.05). The superatoms and cages exhibit "wide but shallow" correlation, while the per-electron correlation density of small clusters is 2–4 times higher.

3. N_D scales extensively with system size, while f_e converges toward characteristic values for each bonding regime: ~ 0.07 for small covalent/metallic clusters and ~ 0.04 for $Cs_3Al_n{}^-$ superatoms.

4. Natural orbital space truncation produces errors of 7× to 6,200× in N_D, with the largest errors occurring for systems where correlation is distributed across many orbitals with individually small deviations from idempotency. Complete occupation data are essential for meaningful N_D calculations.

5. The extensive N_D and intensive f_e provide complementary perspectives: N_D captures the total aggregate correlation across all orbitals, while f_e reveals the intrinsic per-electron correlation character, enabling meaningful comparison across systems with different sizes and core treatments.

6. **Molecular Topology on Quantum Hardware:** Analog simulation on a Rydberg neutral-atom processor using nine molecular graphs demonstrates that different chemical topology classes—aromatic, antiaromatic, cage, and metallic—produce systematically distinct entanglement signatures. Because the Rydberg Hamiltonian is physically distinct from the electronic Hamiltonian, these results characterize the entanglement topology of molecular graphs, not the electronic wavefunction. The observation that entanglement scales with graph connectivity rather than register size suggests that molecular bonding networks encode topological information accessible to analog quantum hardware.

Future work will extend this analysis to additional superatom families (Au, Ag clusters with full CCSD characterization), investigate the dependence of f_e on basis set size, and execute variational quantum eigensolver (VQE) protocols on real neutral-atom hardware

(Pasqal FRESNEL) to move beyond emulator validation. Larger molecular registers (≥ 42 qubits) compatible with FRESNEL device constraints would enable direct hardware noise characterization.

Acknowledgments